H_2O-LiBr Single-Stage Solar Absorption Air Conditioner with an Innovative Bi-Adiabatic Configuration: Dynamic Model, Nominal Conditions and Typical Day Operation

Amín Altamirano, Benoît Stutz, Nolwenn Le Pierrès, and Francis Domain

LOCIE Laboratory, Université Savoie Mont Blanc, CNRS UMR5271, Savoie Technolac, 73376 Le Bourget Du Lac (France)

Abstract

Absorption chillers provide an alternative to conventional compression refrigeration systems as they can run on renewable energy sources and waste heat. However, in the low-capacity range, these systems are more expensive and bulkier when compared with vapor compression systems. Adiabatic exchangers possess a high potential for size reduction in the most limiting components (the absorber and the desorber) through the externalization of the heat transfer in a conventional and compact plate heat exchanger, allowing to perform and enhance the mass transfer in a separate component. The present study proposes a single-stage H_2O-LiBr solar absorption system with an innovative bi-adiabatic configuration, which allows for a wide range of possibilities to enhance the mass transfer, leading to efficient and compact systems. Moreover, only mass-produced standard components would be required. The work is divided into three parts: the first section presents the system's geometry and functioning. The second section includes the dynamic model of the system and its hypothesis. Finally, the third section uses the dynamic model to define the system's operating conditions and evaluates the system coupled to an evacuated tube collector and a simple model of a single-family house under a typical sunny day in the Monterrey (MEX) climate conditions.

Keywords: Absorption chiller, system design, single-stage, dynamic model, adiabatic exchangers

1. Introduction

The global energy demand is expected to increase of 77% from 2000 to 2040 in the New Policies scenario of the International Energy Agency (IEA, 2018a). Considering that 74% of this demand will still be covered by fossil fuels (IEA, 2018a) and other aspects like economic and demographic growth (especially in hot countries), a great challenge is expected for the largest contributor to the world energy consumption and greenhouse emissions: the building sector (Allouhi et al., 2015), whose need for cooling also raises due to the increase in the global average temperature (Aliane et al., 2016). In the building sector, the need for space cooling has more than tripled from 1990 to 2016, and it is still expected to triple by 2050 (IEA, 2018b). Nowadays, in some countries and regions of the Middle East and the United States, space cooling might represent over 70% of peak residential electrical demand during hot days (IEA, 2018b). Therefore, urgent action is needed; especially from governments of countries with a large or potentially large need of cooling, like emerging economies with hot climates, to foresee this problem and avoid important economic and environmental problems (IEA, 2018b).

Absorption chillers provide an alternative to conventional systems and reduce the reliance on fossil fuels (Wu et al., 2014) as they can run on renewable energy sources and waste heat (Dube et al., 2017). These systems replace the standard mechanical compression by a chemical compression and possess different advantages like low operating costs (Wu et al., 2014), higher performance compared with other heat-driven cooling technologies (Hassan and Mohamad, 2012), and operate with natural refrigerants that replace the commonly used hydrofluorocarbons (HFCs) that will be progressively banned under the 2016 Kigali Amendment to the Montreal Protocol (IEA, 2018b). Moreover, when solar-driven, the need for cooling coincides with high irradiance levels (Zhu and Gu, 2010). Nevertheless, in the small-capacity range, these systems present some inconveniences as a high initial investment cost and bulky components, which are both important factors that are directly correlated (Mugnier et al., 2017). Furthermore, special attention is required for small-capacity systems as 70% of the increase in the need for space cooling by 2050 will come from the residential sector (IEA, 2018b).

doi:10.18086/swc.2019.55.01 Available at http://proceedings.ises.org

Nomenclature		*Greek letters*	
A	solar thermal collector area (m^2)	η_0	solar thermal collector optical efficiency
B	solar gain factor (unitless)	η_{col}	solar thermal collector efficiency
a_1	linear coefficient of the solar thermal collector	θ	inclination angle of the solar thermal panel (°)
a_2	quadratic coefficient of the solar thermal collector	*Subscripts and superscripts*	
C_{th}	thermal capacitance (Wh/K)	*a*	absorber
COP	coefficient of performance	*abs*	absorption
G^*	global horizontal solar irradiance (Wm^{-2})	*ad*	adiabatic
h	specific enthalpy (kJ kg−1)	*amb*	ambient
$k(\theta)$	solar thermal collector tilt angle factor	*c*	condenser
M	stored mass (kg)	*col*	collector
$\dot{m}$	mass flow rate (kg s^{-1})	*e*	evaporator
$\dot{Q}$	exchanged heat (kW)	*g*	generator
R_{th}	thermal resistance (K/W)	*htf*	heat transfer fluid
T	temperature (K)	*i*	in
T_m	average temperature of the fluid in the solar collector (K)	*m*	mass
$\dot{W}$	mechanical work transfer to or from the component (kW)	*max*	maximum
x	absorbent solution mass fraction	*o*	out
		p	pump
		sol	solution
		sorp	sorption
		th	thermal

Therefore, there is a need to reduce the cost and increase the compactness of small-capacity absorption systems. At the machine level, the main cost reduction potential is considered to be in the manufacturing costs reduction and mass-scale production (IEA, 2018b; Mugnier et al., 2017). The last option can be hardly assessed as it depends on the demand, which cannot increase unless some economic, demographic, governmental, and manufacturing aspects are gathered together. As for the first option, the heat and mass exchangers have been pointed out as the limiting components in terms of size, performance, and cost; especially for the absorber (Beutler et al., 1996; Kays and London, 1984). On this direction, adiabatic exchangers have gained attention in recent years as they could lead to compact, low-weight, and low-cost systems, through the separation of heat and mass transfers into two steps (Gutiérrez-Urueta et al., 2012; Venegas et al., 2003; Ventas et al., 2010). Usually, a conventional plate heat exchanger is used for the heat transfer owing to its high compactness (Wang et al., 2007) and the mass transfer is performed in a different chamber where the solution can be distributed or dispersed in different forms to absorb or desorb refrigerant vapor. This allows for an immense number of possibilities to enhance the exchange area and generate flow instabilities, leading to high performance and compactness.

For the reasons exposed before, a new geometry of a single-stage H_2O-LiBr absorption cooling system with a bi-adiabatic configuration is proposed. H_2O-LiBr was selected as the working pair since it is until now the most efficient and reliable working fluid for positive cooling. This new architecture would not only lead to high compactness but also to avoid on-demand production by selecting only mass-produced standard heat exchangers. The present study is divided into three parts. In the first section, the proposed machine architecture is presented and discussed. In the second section, the description of the dynamic model based on the mass and energy balances of the components and with a definition of the mass effectiveness is presented. Finally, in the last section, the dynamic model is used to identify the optimum operating conditions of the system and evaluate its operation for a typical summer day using real data from 2018 of the Monterrey (MEX) city. The typical day operation was performed by coupling the system with the model of an evacuated tube collector and a single-family house.

2. System description

An absorption chiller in its simple form comprises an evaporator, a condenser, a non-adiabatic absorber, a non-adiabatic generator (also called desorber), a solution pump, a solution heat exchanger, and two expansion valves. However, the present paper studies a new configuration of H_2O-LiBr absorption heat pump whose main innovation can be found in the fully adiabatic sorption process (absorption and desorption, see Figure 1). In this case, the heat transfer is performed in a conventional single-phase heat exchanger (HX_g for the generator, and HX_a for the absorber) and the mass transfer is performed in a separate adiabatic mass exchanger (MX_g and MX_a) that allows innovative distribution methods or surface geometries to enhance the mass transfer.

In the proposed configuration, the diluted solution at the HX_g is superheated by the heat transfer fluid (HTF) and then sent to the adiabatic generator (MX_g), where the adiabatic desorption of refrigerant vapor happens. The desorbed refrigerant vapor goes through the condenser and once in the liquid phase it goes through the refrigerant expansion valve (*REV*) before being evaporated at low pressure in the evaporator, where the cooling effect takes place. A refrigerant recirculation in the evaporator is generated by means of a pump (P_3). The vapor generated is then sent to the adiabatic absorber (MX_a) where it is absorbed by the concentrated solution (that has already been pre-cooled in the HX_a). The resulting solution goes to the solution storage tank and the mixed solution is pumped by P_1 to the generator, where the cycle starts again. To increase the efficiency of the system with internal heat recovery, a solution heat exchanger (*SHX*) is placed between the absorber and the generator. Moreover, two recirculation pumps are added (P_2 and P_4) to increase the system's performance.

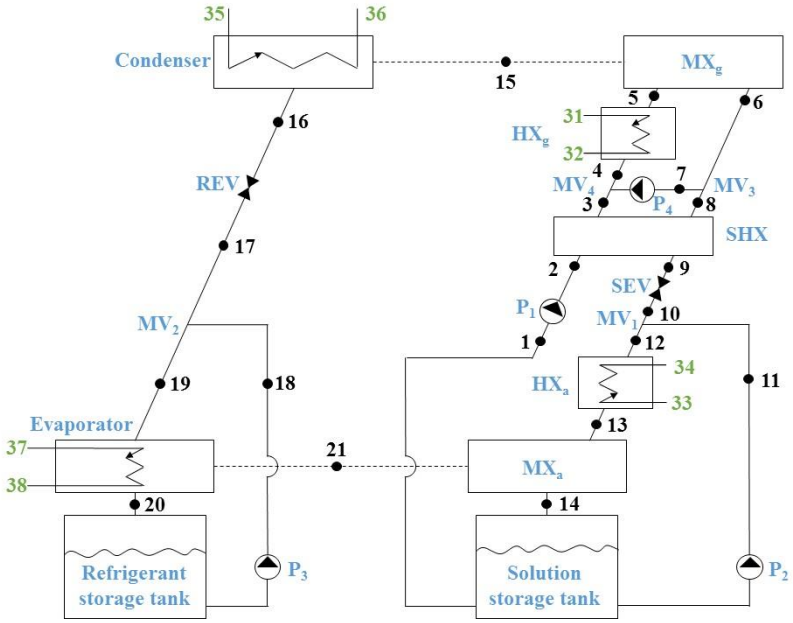

Fig. 1: H_2O-LiBr single effect bi-adiabatic absorption chiller.

3. Dynamic model

The study of the dynamic behavior of absorption chillers is of great importance owing to their high response time compared with conventional compression chillers of a similar capacity. This is in part due to the thermal inertia of their components and the liquid accumulation in them (Evola et al., 2013; Kohlenbach and Ziegler, 2008; Ochoa et al., 2016). In the present case, the state points represented in Figure 1 show the different internal thermodynamic conditions of the H_2O-LiBr solution (1-14), the water vapor (15 and 21), and the liquid water (16-20). Moreover, the green numbers represent the external thermodynamic states of the heat source (31 and 32), the cooling source (33-36), and the chilled source (37 and 38). The developed model is based on the mass and energy balances of each component. The thermodynamic properties of the H_2O-LiBr working pair were obtained from Yuan and Herold (2005). Finally, the simplifying assumptions taken into account in the model are as follows:

- There are no heat transfers with the ambient temperature.
- The refrigerant and solution in the storage tanks are fully mixed.
- The expansion valves are isenthalpic and the pumps are isentropic.
- The vapor at the output of the adiabatic generator is in equilibrium with the concentration of the solution at point 5 [$T_{15} = T_{eq}(P_h, x_5)$].
- The refrigerant is at saturation state at the output of the condenser and the evaporator.
- The characteristic time of the components is neglected with regards to the characteristic time of the storage tanks and the transport delay between them.
- The thermal inertia of the system's components is neglected.

Different dynamic simulations are present in the literature. In most of the cases, the performance of the heat and mass transfer exchangers is characterized by a thermal effectiveness and the solution is considered in equilibrium with the

outlet temperature and the operating pressure (Aiane et al., 2017); however, this is never the case in real operating systems. For this reason, in the present model, the exchangers' performance is defined by their thermal or mass effectiveness ($\mathcal{E}_{th}$ *or* $\mathcal{E}_m$, respectively). The thermal effectiveness of the heat exchangers (condenser, evaporator, *SHX*, HX_g, and HX_a) is the same as the one of conventional single-phase and phase change exchangers defined as the ratio of the real transferred heat to the maximum theoretical transferable heat with the same input conditions (equation 1). On the other hand, for the adiabatic exchangers (MX_a and MX_g), the mass effectiveness is defined as the ratio of the actual exchanged mass (absorbed or desorbed mass) to the maximum theoretical transferable mass of sorption under the same input conditions (equation 2) (Patnaik and Perez-Blanco, 1994; Islam et al., 2006). The procedure used for calculating the mass effectiveness in the case of the absorber was described in (Michel et al., 2017). For the present study, as both sorption processes are of adiabatic type, the mass effectiveness in the absorption mode is calculated by solving equations (2-6), and a similar procedure is applied in the case of the generator.

$$\varepsilon_{th} = \frac{\dot{Q}}{\dot{Q}_{max}} \quad \text{(eq. 1)}$$

$$\varepsilon_m = \frac{\dot{m}_{sorp}}{\dot{m}_{sorp}^{max}} \quad \text{(eq. 2)}$$

$$\dot{m}_{sol,i} + \dot{m}_{abs,ad}^{max} - \dot{m}_{sol,o} = 0 \quad \text{(eq. 3)}$$

$$\dot{m}_{sol,i} x_{sol,i} - \dot{m}_{sol,o} x_{sol,o} = 0 \quad \text{(eq. 4)}$$

$$\dot{m}_{sol,i} h_{sol,i} + \dot{m}_{abs,ad}^{max} h_{vap} - \dot{m}_{sol,o} h_{sol,o} = 0 \quad \text{(eq. 5)}$$

$$T_{sol,o}^{ad} = T_{sol,o}\left(h_{sol,o}; P_{abs}; x_{sol,o}\right) = T_{sol,eq}\left(P_{abs}; x_{sol,o}\right) \quad \text{(eq. 6)}$$

A constant transport delay (t) of the solution and refrigerant was considered between every state point so that the properties at the output of each component were calculated with the outputs of the precedent component at a time $-t$. Moreover, the equilibrium condition in the desorbed/condensed ($\dot{m}_{des} = \dot{m}_{cond}$) and evaporated/absorbed ($\dot{m}_{ev} = \dot{m}_{abs}$) vapor is always fulfilled. The mass and energy balances of each component are described by equations (7-9).

$$\sum \dot{m}_i = \sum \dot{m}_o \quad \text{(eq. 7)}$$

$$\sum (\dot{m}_i x_i) = \sum (\dot{m}_o x_o) \quad \text{(eq. 8)}$$

$$\sum ((\dot{m}_i h_i) - (\dot{m}_o h_o)) + \sum (\dot{Q}_i - \dot{Q}_o) + \dot{W} = 0 \quad \text{(eq. 9)}$$

As mentioned before, absorption systems usually have a higher response time compared with conventional vapor compression systems; however, for small-capacity systems, the thermal inertia of the components and the liquid mass stored in them have a much lower impact. Therefore, in these conditions, the transport delay and the liquid mass content in the storage tanks are the elements that most impact the response time. The storage tanks' behavior is described by equations (10-12).

$$\frac{d(M_{st})}{dt} = \sum \dot{m}_i - \sum \dot{m}_o \quad \text{(eq. 10)}$$

$$\frac{d(M_{st} x_{st})}{dt} = \sum (\dot{m}_i x_i) - \sum (\dot{m}_o x_o) \quad \text{(eq. 11)}$$

$$\frac{d(M_{st} h_{st})}{dt} = \sum (\dot{m}_i h_i) - \sum (\dot{m}_o h_o) \quad \text{(eq. 12)}$$

A recirculation rate was defined at the generator and the absorber which defines $\dot{m}_{p2}$ and $\dot{m}_{p4}$ as functions of $\dot{m}_{p1}$, as shown in equation (13). Another important parameter is the thermal COP, which is defined by equation 14.

$$R = \frac{\dot{m}_{p2}}{\dot{m}_{p1}} = \frac{\dot{m}_{p4}}{\dot{m}_{p1}} \quad \text{(eq. 13)}$$

$$COP_{th} = \frac{\dot{Q}_e}{\dot{Q}_g} \quad \text{(eq. 14)}$$

Finally, a second law analysis was performed to identify the most exergy destructive components. The exergy, defined as the maximum work potential of a material or an energy stream compared to its surrounding environment, is defined by equation (15) (KOTAS, 1985), in which h and s are the enthalpy and entropy of the fluid and h_0 and s_0 are the enthalpy and entropy of the same fluid at the ambient temperature and pressure. The exergy destruction (ED) by component is given by equation (16). Therefore, the total system exergy destruction is the sum of the exergy destruction in all its components.

$$\psi = (h - h_0) - T_0(s - s_0) \quad \text{(eq. 15)}$$

$$\Delta\psi = \sum(\dot{m}_i\psi_i) - \sum(\dot{m}_o\psi_o) \qquad \text{(eq. 16)}$$

4. Results and discussion

4.1 System's optimum operating conditions

The aim of the present section is to determine the optimum operating conditions of the proposed system with a nominal cooling capacity of 5 kW. The HTF in the different heat exchangers is assumed to be water. Therefore, considering a $\Delta T = 5°C$ for the HTF in the evaporator, a $\dot{m}_{37} = 0.24$ kg/s was calculated. The same value was attributed to $\dot{m}_{35}$ as the condenser would operate at similar capacities. $\dot{m}_{p3}$ was calculated according to the need of a minimum flow rate required to have an acceptable performance on a helical falling film heat exchanger with a coil diameter of 30 cm. A minimum flow rate of 1 l/min was considered per meter of coil perimeter, which led to a $\dot{m}_{p3} = 0.016$ kg/s. Finally, for the purposes of the study, constant HTF inlet temperatures at the evaporator and the condenser were defined at $T_{35} = 15°C$ and $T_{37} = 30°C$, respectively. Regarding the heat exchangers, a constant thermal efficiency of 0.8 was selected for the condenser, the evaporator, and the *SHX*. In the case of the HX_g and HX_a, as their capacities would vary depending on the operating conditions at steady-state, it is more practical at this stage to define a pinch of 3°C between the output of the solution and the inlet of the HTF ($Pinch_g = T_{31} - T_5 = 90 - 87°C$ and $Pinch_a = T_{13} - T_{33} = 33 - 30°C$).

A parametric study was performed to identify the optimum operating conditions of the system. This procedure was mainly based on two different parameters: the $\dot{m}_{p1}$ and R. For every $\dot{m}_{p1}$, the program would start at a very low R and run until the stabilization condition is achieved ($\dot{m}_{ev} = \dot{m}_{cond}$), R was iteratively increased until reaching the 5 kW set point capacity at the evaporator. Two scenarios were studied: one with $\mathcal{E}_m = 0.4$ for both adiabatic exchangers and another one with $\mathcal{E}_m = 0.6$. Results can be observed in Figure 2. From this Figure, two acceptable $COP_{th,min}$ were considered (0.7 and 0.75). For a $COP_{th,min} = 0.7$, $\dot{m}_{p1} = 0.075$ kg/s and R = 10 would be required with $\mathcal{E}_m = 0.4$, while R = 6.25 is required with $\mathcal{E}_m = 0.6$. On the other hand, for $COP_{th,min} = 0.75$, $\dot{m}_{p1}$ of around 0.05 kg/s is required with R = 17.3 and $\mathcal{E}_m = 0.4$, and R = 11 with $\mathcal{E}_m = 0.6$. It's worth mentioning that in none of those conditions there was a risk of crystallization.

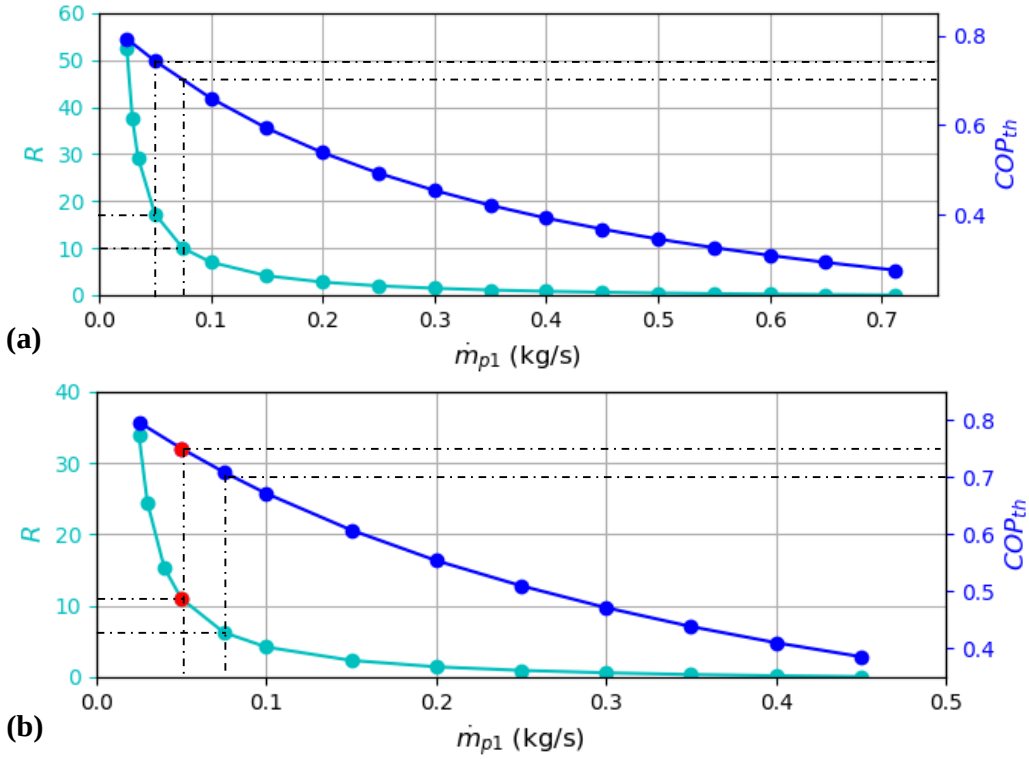

Fig. 2: Thermal COP and R vs $\dot{m}_{p1}$ for a (a) $\mathcal{E}_m = 0.4$ and (b) $\mathcal{E}_m = 0.6$ in the mass exchangers (● nominal conditions).

Taking into consideration the system stability and electric consumption limitation due to the pumps work, an R close to 10 or less is preferable. Under these conditions, a $\mathcal{E}_m = 0.4$ would only be accepted by reducing the $COP_{th,min}$ to 0.7, while a $\mathcal{E}_m = 0.6$ would be preferable to obtain a thermal *COP* of 0.75; therefore, this last condition was selected as the nominal operating state of the machine ($COP_{th} = 0.75$ // $\dot{m}_{p1} = 0.05$ kg/s // $\mathcal{E}_m = 0.6$ // R = 11). Once this

condition selected, a calculation of the HX_g and HX_a thermal effectiveness was performed (equations (17-18)) with the rest of the parameters of the simulated results ($\dot{Q}_g$ = 6.67 kW // $\dot{Q}_a$ = 6.64 kW // $T_4/T_5/T_{31}$ = 81.47/87/90°C // $T_{12}/T_{13}/T_{33}$ = 38.37/33/30°C).

$$\varepsilon_{th,g} = \frac{T5-T4}{T31-T4} = 0.65 \qquad \text{(eq. 17)}$$

$$\varepsilon_{th,a} = \frac{T12-T13}{T12-T33} = 0.64 \qquad \text{(eq. 18)}$$

The thermal efficiencies are acceptable considering that for the other heat exchangers a $\mathcal{E}_{th}$ = 0.8 was taken into account. Finally, the required HTF flow rates are calculated (equations (19-20)) for both heat exchangers assuming a ΔT = 5°C for the HTF in both exchangers, a water Cp at 88.5°C for the HX_g, and a Cp at 28.5°C for the HX_a, which corresponds to 4202.81 and 4177.35 $Jkg^{-1}K^{-1}$, respectively.

$$\dot{m}_{htf,g} = \frac{Qg}{Cp*\Delta T} = \frac{6670}{4202.81*5} = 0.31725\ \frac{kg}{s} \qquad \text{(eq. 19)}$$

$$\dot{m}_{htf,a} = \frac{Qa}{Cp*\Delta T} = \frac{6640}{4177.35*5} = 0.3065\ \frac{kg}{s} \qquad \text{(eq. 20)}$$

Therefore, the nominal external parameters were defined as follows: $\dot{m}_{htf,g}$ = 0.32 kg⁄s; $T_{htf,g}$ = 90°C; $\dot{m}_{htf,a}$ = 0.31 kg⁄s; $T_{htf,a}$ = $T_{htf,c}$ = 30°C; $\dot{m}_{htf,c}$ = $\dot{m}_{htf,e}$ = 0.24 kg⁄s, $T_{htf,e}$ =15°C, and the internal parameters were defined as: $\dot{m}_{p1}$ = 0.05 kg⁄s; $\dot{m}_{p2}$ = $\dot{m}_{p4}$ = R*$\dot{m}_{p1}$ = 0.55 kg⁄s; $\dot{m}_{p3}$ = 0.015 kg/s. These parameters with the selected and calculated thermal efficiencies ($\mathcal{E}_{th,e}/\mathcal{E}_{th,c}/\mathcal{E}_{th,shx}$=0.8 and $\mathcal{E}_{th,g}$=0.65/$\mathcal{E}_{th,g}$=0.64) provide 5 kW of cooling with a thermal COP of 0.75. However, considering the implementation of PHE in all the thermal components and that this type of exchanger can easily achieve efficiencies of 0.8, a nominal thermal efficiency of 0.8 for all the components was selected. With this improved efficiency in the HX_a and the HX_g, the chiller would provide a cooling power of 5.4 kW with a COP of 0.751.

4.2 Typical day operation

Once the nominal conditions defined, the system was studied under real simulated conditions coupled to an evacuated tube collector as the high-temperature source, a single-family house in the Monterrey (MEX) climate conditions as the low-temperature source, and a helical geothermal heat exchanger (GHX) as the intermediate-temperature source (Figure 3a). The Monterrey's Integral System of Environmental Monitoring provided data of the global solar horizontal irradiance and the ambient temperature of the Monterrey city (SIMA, 2019). Data from the 23 July 2018 were used as it is a representative summer day in Monterrey (Figure 3b). From this data, the selected evaluation period was from 6 A.M. to 8 P.M. as outside this period there is no irradiance.

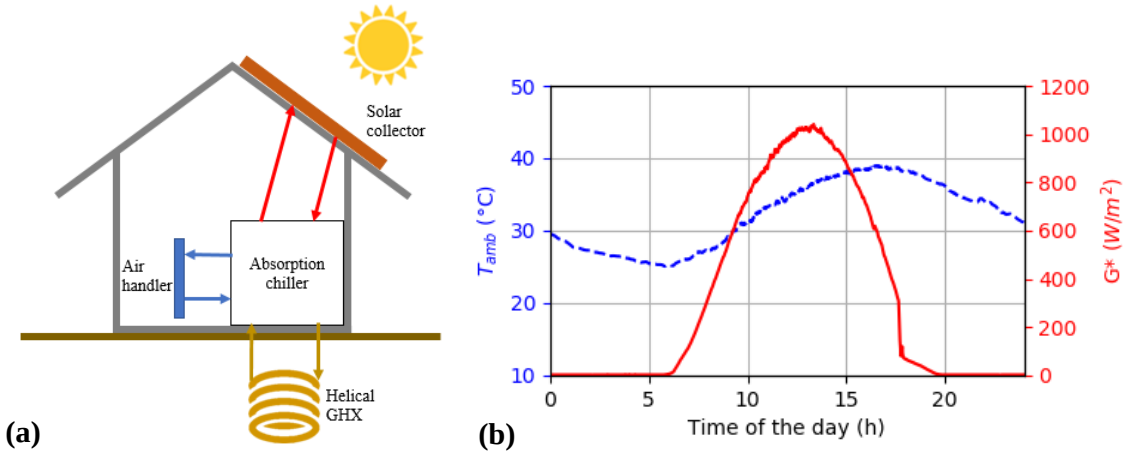

Fig. 3: (a) Diagram of the integrated solar-geothermal absorption cooling system (adapted from (Altamirano et al., 2018) and (b) Monterrey city climate conditions of the 23 July 2018 (SIMA, 2019).

The simulated collector corresponds to the Thermomax-Mazdom vacuum tube collector, whose performance is defined by equations (21-23) and with the following properties: η_0 = 0.804, a_1 = 1.15 °C·m²kW⁻¹ and a_2 = 0.0064 °C·m²kW⁻¹ (Vargas Bautista et al., 2011). Moreover, the collector was considered to have a tilt angle of 25°, south orientation (recommended for Monterrey's 25° 4' north latitude) (Vargas Bautista et al., 2011), and an area of 10.5 m².

$$\dot{Q}_g = A \cdot G^* \cdot \eta_{col} \qquad \text{(eq. 21)}$$

$$\eta_{col} = k(\theta) \cdot \eta_0 - a_1 \frac{T_m - T_{amb}}{G^*} - a_2 \frac{(T_m - T_{amb})^2}{G^*} \quad \text{(eq. 22)}$$

$$k(\theta) = 1 - 0.239 \left(\frac{1}{cos\theta} - 1\right) \quad \text{(eq. 23)}$$

Considering that the intermediate temperature source is composed by helical GHXs and assuming that the variation of the ground temperature is negligible in the simulated period of time (14 h), a parallel flow was considered for the absorber and the condenser with a constant HTF inlet temperature of 30°C, which is reasonable for the Monterrey climate conditions (Altamirano et al., 2018). Finally, the house was simulated through a simple model based on an equivalent thermal resistance, capacitance, and solar gain factor (1R1C + solar gain, see Figure 4c and eq. (24)) whose parameters (R_{th} = 0.01282 K/W, C_{th} = 5380 Wh/K, and B = 5, respectively) were obtained after a characterization study based on experimental temperatures and irradiance measurements obtained from a single-family house with a wooden structure (see Figure 4a and b), good insulation and good thermal inertia (Domain et al., 2015). The house is a two-floor house with 218 m^2 of wall surface, 60 m^2 of ground surface, 18 m^2 of windows' surface, and a total volume of around 240 m^3. Only the irradiance on the south side of the house was taken into account as it contains the largest windows area (15 m^2) and the east and west side irradiances are mostly blocked by trees.

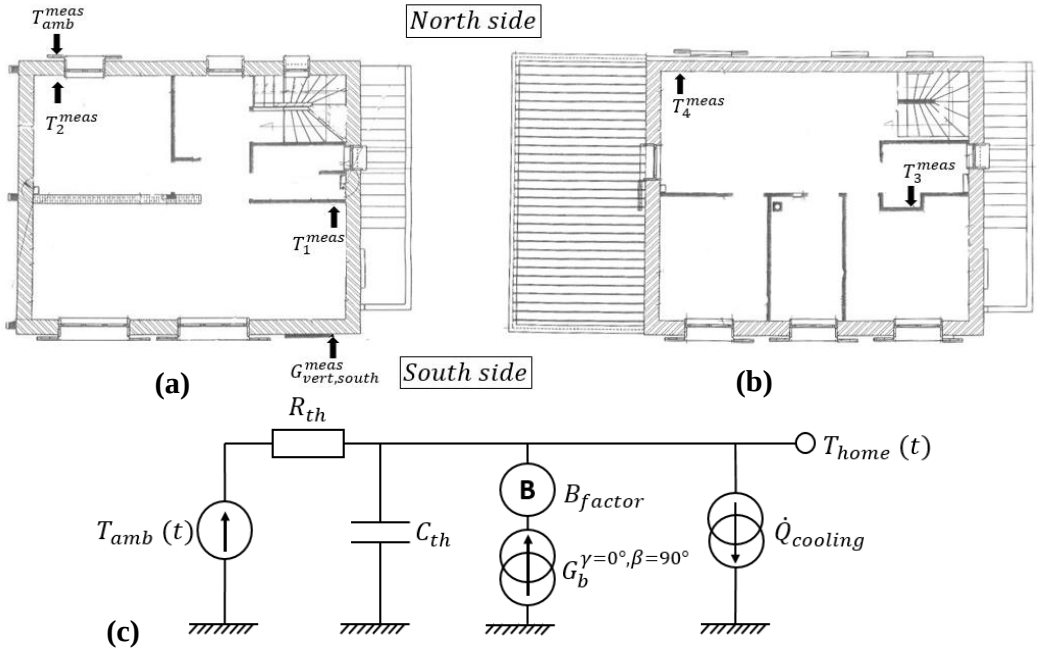

Fig. 4: Studied single-family house. (a) Ground floor and (b) first floor plans, and (c) 1R1C thermal model considering the cooling power and irradiance on the south face.

$$\frac{d(T_{home}(t))}{dt} = \frac{B \cdot G^*_{vert,south}(t) + \left[(T_{amb}(t) - T_{home}(t))/R_{th}\right] - \dot{Q}_{cooling}(t)}{C_{th}} \quad \text{(eq. 24)}$$

The chiller was considered to operate at steady-state at the beginning of the simulation (6:00 A.M.) with the parameters defined in section 4.1 except for the external inlet temperatures, which were defined as follows: an intermediate temperature ($T_{33} = T_{35}$) of 30°C coming from a geothermal source, an initial low-temperature (T_{37}) equal to the ambient temperature (25.2°C), and a driving temperature (T_{31}) equal to the cut-off temperature (temperature necessary for the system to generate a cooling effect) of those conditions (33.5°C). The initial home ambient temperature was that of the ambient temperature (25.2°C). Figure 5 shows the evolution of the absorption system's external temperatures, the ambient temperature, and the home temperature with (T_{home1}) and without (T_{home2}) the effect of the chiller's cooling power. As there are no external thermal storage tanks to absorb the temperature variations of the hot and cold sources, their temperatures follow the sources' conditions achieving around 86°C at the hot transfer fluid and 6.2 kW of cooling capacity (Figure 6). At the beginning there was not enough cooling power to compensate for the heat exchange with the ambient temperature and the solar gain; therefore, the home temperature slowly increased by up to 1°C until 9:00 A.M. After that, the house is effectively cooled by the absorption chiller achieving a temperature as low as 21.5°C until 17:30 hours, and maintaining a temperature lower than 22°C until the end of the day. Without the cooling power, the internal home temperature is highly affected by the ambient temperature and the solar gain, achieving a temperature of 30.6°C by the end of the day, which makes a

temperature difference of almost 9°C compared with the cooled case. Using the absorption chiller, temperature conditions in the thermal comfort range according to the ANSI/ASHRAE Standard 55-2004 (ASHRAE, 2004) are always achieved, which is not the case for the non-cooled case. Finally, the system provided 46.5 kWh of cooling for 61.3 kWh at the generator and 108.5 kWh at the intermediate source, leading to a cumulative COP (integrated cooling capacity by the integrated heat input (Lazzarin, 1980)) of 0.765.

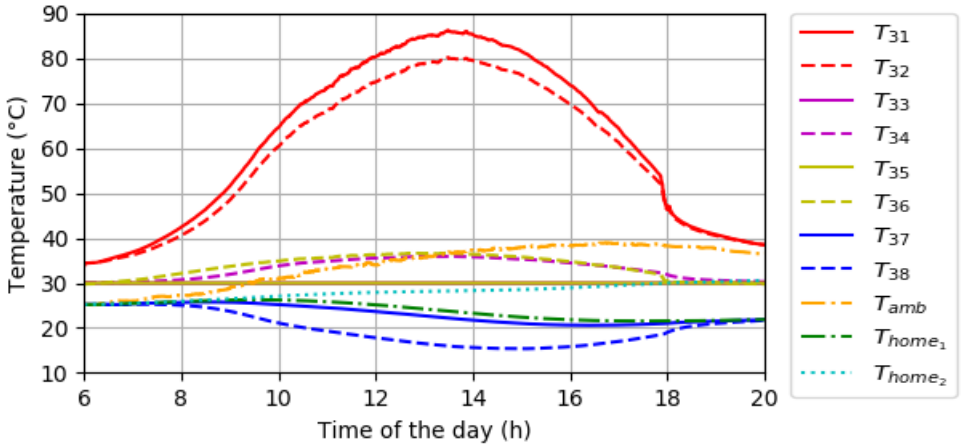

Fig. 5: Evolution of the absorption chiller's external temperatures, the ambient temperature, and home temperature with and without the cooling power.

The inlet-outlet temperature differences in Figure 5 represent the exchanged heat for each component in the system, which is better represented in Figure 6. This figure shows that at full irradiation, the absorber and generator heat exchangers are the ones with the higher values, followed by the condenser and the evaporator. At the end of the day, when the solar irradiation decreases, the heat exchanged at the generator and the condenser drops lower than that of the absorber and the evaporator, respectively, at around 15:30 hours. This is because, at the low-pressure stage, the thermal inertia in the solution and refrigerant storage tanks play an important role in the cooling generation. This is even more accentuated at around 18:00 hours, when clouds arrive over the zone and there is a sudden drop in the solar irradiance (Figure 3b), drastically decreasing the generator temperature and increasing the exchanged heat difference between the two stages. The heat exchanged at the SHX is low at full operating conditions owing to the recirculation implemented in the absorber and the generator. However, as the solar irradiance decreases, this exchanged heat becomes predominant as the temperature difference between the intermediate and hot temperature sources is still considerable while the low cooling production regime (low absorption and desorption rates) leads to a low heat exchange in the rest of the exchangers.

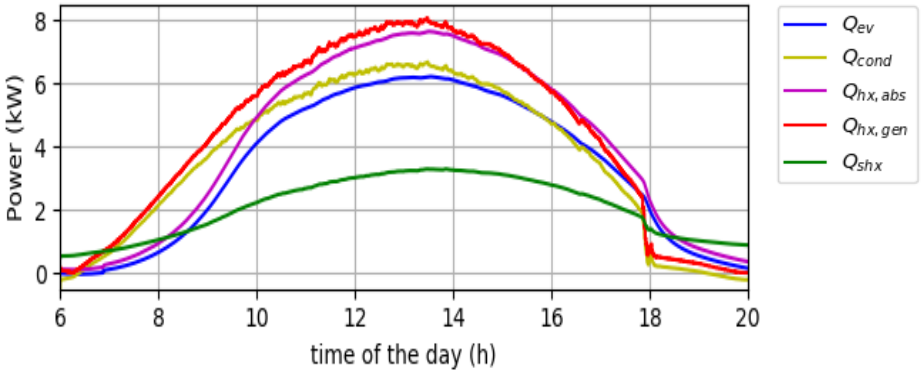

Fig. 6: Evolution of the heat exchanged in the different components of the absorption system for the studied period.

Figure 7 shows the evolution of the content in the storage tanks and the concentrations at the inlet and outlet of the absorber and the generator. A short stabilization period is observed before 7:00 hours, in which the irradiance is not sufficient to provide a temperature high enough to generate a desorption effect. Therefore, an absorption process happens, and the condenser evaporates for a short period. This can also be observed in Figure 8, with a small period of negative condensed mass ($\dot{m}_{15}$). As the driving temperature source increases, the solution circuits increase in concentration to follow the new equilibrium conditions. This is better observed by the decrease in the content of the solution storage tank and the increase in water content in the refrigerant storage tank between 7:00 and 14:00 hours

(Figure 7). As the generator temperature increases, the equilibrium concentration also increases and therefore, the difference in concentration between the absorber and the generator also increases, achieving a maximum concentration at the generator of 0.55, which does not imply a risk of crystallization.

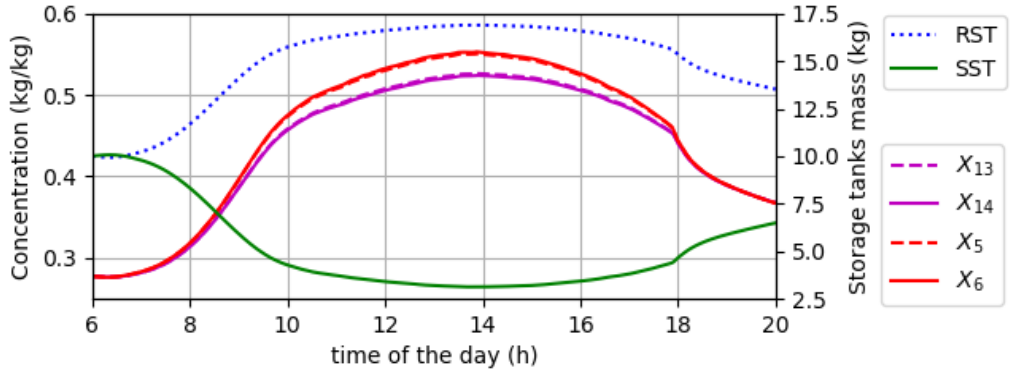

Fig. 7: Evolution of the (a) mass contained in the solution and refrigerant storage tanks and the (b) inlet-outlet solution concentrations at the absorber and desorber.

As mentioned before, the sudden drop in the solar irradiance of around 18:00 hours drastically affects the machine behavior decreasing the generator and condenser heat exchanges, and therefore affecting the condensed vapor, as observed in Figure 8. After 19:00, the provided generator temperature is not sufficient anymore to desorb water vapor. However, the cooling generation continues thanks to the thermal inertia of the storage tanks, and this can be observed in the positive evaporated mass ($\dot{m}_{21}$).

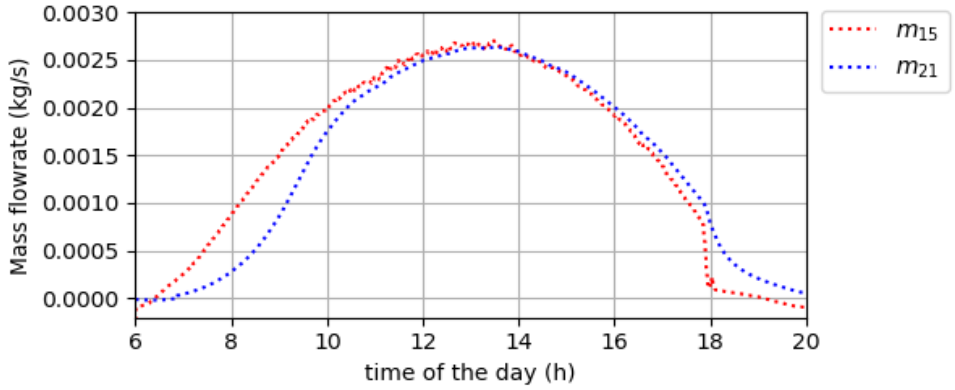

Fig. 8: Condensed ($\dot{m}_{15}$) and evaporated ($\dot{m}_{21}$) mass flow rates for the studied period.

Another figure of interest is the high and low pressures in the absorption system, which are shown in Figure 9. An important influence of the generator (directly related to the solar irradiance) and evaporator temperatures can be observed, achieving a maximum high pressure of around 6.75 kPa and a minimum low pressure of around 1.59 kPa. The impact of the solar irradiance on the operating pressures can also be observed in the sudden pressure drop that happens when the available solar irradiance decreases at around 18:00 hours.

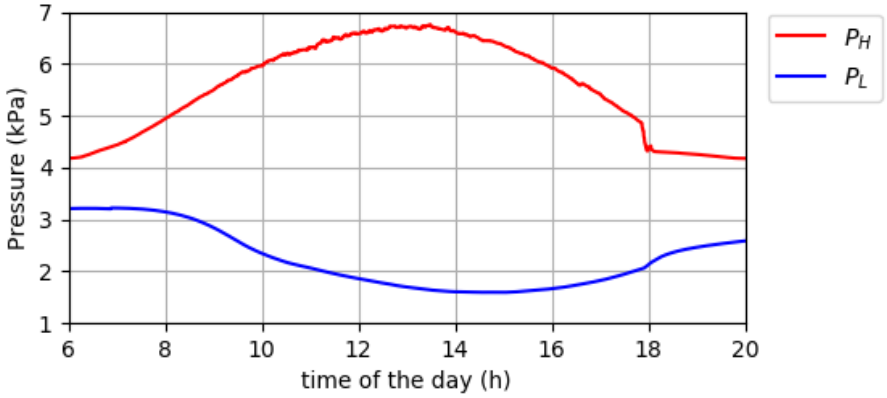

Fig. 9: Operating pressures in the system for the studied period.

Finally, Figure 10 shows the exergy destruction in the main components and the total system's exergy destruction. At the beginning of the studied period, the components that destruct the most exergy are the condenser and the evaporator. This is because the enthalpy of vaporization/condensation plays an important role in these operating conditions compared with the single-phase exchangers and the enthalpy of mixing in the adiabatic sorption processes, especially for the condenser that, as described by the model, receives superheated vapor. However, as the generator temperature increases, the circulated refrigerant vapor increases and the concentration difference in the adiabatic absorber/generator becomes higher. In these conditions, the heat of mixing and the low mass efficiency in the adiabatic absorber/desorber become the predominant factor for the exergy destruction, especially for the generator that operates at higher temperatures. At full operation, the adiabatic generator is the component that destructs the most exergy, followed by the adiabatic absorber, the condenser, the evaporator, the *SHX*, the HX_a, and the HX_g.

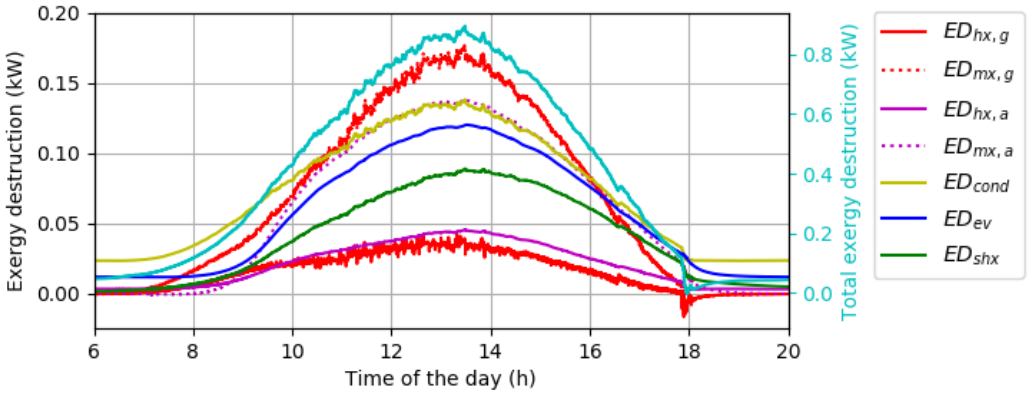

Fig. 10: Exergy destruction in the main components and total exergy destruction.

5. Conclusions and perspectives

A first and second law dynamic model of a bi-adiabatic small-capacity absorption chiller based on its components' thermal and mass efficiencies was developed and used to identify its nominal conditions and to study its behavior coupled to a solar thermal collector as the high temperature source, a helical geothermal heat exchanger as the intermediate temperature source, and a single-family house.

A configuration like the one presented here can deliver cooling capacities to a single-family house that would lead to comfortable room temperatures and with a temperature difference of around 9°C compared with a non-cooled home. In the present study, the system provided up to 6.2 kW of cooling and a cumulative COP of 0.77. Moreover, there was no risk of crystallization in the studied conditions.

The dimensioning of the solution and refrigerant storage tanks are of great importance to reduce the response time of the system but at the same time, a compromise must be found to give some thermal inertia to the system to smooth the variations of the external conditions.

Finally, the exergetic study showed that the components that lead to the highest exergy destruction are the adiabatic desorber and absorber, respectively. This is due to the low mass efficiencies that were selected for these components and to the impact of the enthalpy of mixing. Therefore, special attention has to be paid to design adiabatic absorbers and desorbers with an elevated mass efficiency. The next step will be the design, construction, and experimental characterization of new adiabatic exchangers that would provide at least the nominal mass efficiencies presented in this study.

6. Acknowledgements

The authors would like to thank the Mexican sectorial fund "CONACYT-SENER-SUSTENTABILIDAD ENERGÉTICA" and the PACs-CAD project for their support to this research. "PACs-CAD" is a cross-border project supported by Interreg France-Switzerland, a European territorial cooperation program. It has received 463,185 € through the European regional development fund (ERDF) and 150,000 CHF through the Swiss Federal Interreg funds.

7. References

Aiane, M., Ramousse, J., Bouyaud, M., Boudard, E., Stutz, B., 2017. Modélisation dynamique d'un système de climatisation par absorption, in: Congrès Société Française de Thermique, 30 May - 2 Juin. Marseille, France.

Aliane, A., Abboudi, S., Seladji, C., Guendouz, B., 2016. An illustrated review on solar absorption cooling experimental studies. Renew. Sustain. Energy Rev. 65, 443–458. https://doi.org/10.1016/j.rser.2016.07.012

Allouhi, A., Fouih, Y. El, Kousksou, T., Jamil, A., Zeraouli, Y., Mourad, Y., 2015. Energy consumption and efficiency in buildings : current status and future trends. J. Clean. Prod. 109, 118–130. https://doi.org/10.1016/j.jclepro.2015.05.139

Altamirano, A., Stutz, B., Le Pierrès, N., 2018. Selection of High-Performance Working Fluid for a Solar-Geothermal Absorption Cooling System and Techno-Economic Study in the Northern Mexican Conditions, in: 12th International Conference on Solar Energy for Buildings and Industry, September 10-13. Rapperswil, Switzerland.

ASHRAE, 2004. ANSI/ASHRAE Standard 55-2004: Thermal Environmental Conditions for Human Occupancy.

Beutler, A., Hoffmann, L., Ziegler, F., Alefeld, G., Gommed, K., Grossman, G., Shavit, A., 1996. Experimental Investigation of Heat and Mass Transfer on Horizontal and Vertical Tubes, in: Proceedings of the International Absorption Heat Pump Conference, September 17-20. Montreal, Canada, pp. 409–419.

Domain, F., Brabant, A., Souyri, B., Stutz, B., 2015. Estimation du comportement du bâti par analogie électrique RC - Application au délestage électrique, in: JNES. Perpignan, France.

Dube, E., Cha, A., Agboola, O.P., Or, J., Fakeeha, A.H., Al-fatesh, A.S., 2017. Energetic and exergetic analysis of solar-powered lithium bromide- water absorption cooling system. J. Clean. Prod. 151, 60–73. https://doi.org/10.1016/j.jclepro.2017.03.060

Evola, G., Le Pierrès, N., Boudehenn, F., Papillon, P., 2013. Proposal and validation of a model for the dynamic simulation of a solar-assisted single-stage LiBr/water absorption chiller. Int. J. Refrig. 36, 1015–1028. https://doi.org/10.1016/j.ijrefrig.2012.10.013

Gutiérrez-Urueta, G., Rodríguez, P., Ziegler, F., Lecuona, A., Rodríguez-Hidalgo, M.C., 2012. Extension of the characteristic equation to absorption chillers with adiabatic absorbers. Int. J. Refrig. 35, 709–718. https://doi.org/10.1016/j.ijrefrig.2011.10.010

Hassan, H.Z., Mohamad, A.A., 2012. A review on solar cold production through absorption technology. Renew. Sustain. Energy Rev. 16, 5331–5348. https://doi.org/10.1016/j.rser.2012.04.049

IEA, 2018a. World energy outlook.

IEA, 2018b. The Future of Cooling.

Islam, M.R., Wijeysundera, N.E., Ho, J.C., 2006. Heat and mass transfer effectiveness and correlations for counter-flow absorbers. Int. J. Heat Mass Transf. 49, 4171–4182. https://doi.org/10.1016/j.ijheatmasstransfer.2006.04.002

Kays, W.M., London, A.L., 1984. Compact heat exchanger. New York: McGraw-Hill.

Kohlenbach, P., Ziegler, F., 2008. A dynamic simulation model for transient absorption chiller performance. Part I: The model. Int. J. Refrig. 31, 217–225. https://doi.org/10.1016/j.ijrefrig.2007.06.009

KOTAS, T., 1985. The exergy method of thermal plant analysis. Great Britain: Anchor Brendon Ltd.

Lazzarin, R., 1980. Steady and transient behaviour of LiBr absorption chillers of low capacity. Rev. Int. du Froid 3, 213–218.

Michel, B., Le Pierrès, N., Stutz, B., 2017. Performances of grooved plates falling film absorber. Energy 138, 103–117. https://doi.org/10.1016/j.energy.2017.07.026

Mugnier, D., Neyer, D., White, S., 2017. The Solar Cooling Design Guide: Case Studies of Successful Solar Air Conditioning Design. Ernst & Sohn.

Ochoa, A.A. V, Dutra, J.C.C., Henríquez, J.R.G., Santos, C.A.C., 2016. Dynamic study of a single effect absorption chiller using the pair LiBr/H_2O. Energy Convers. Manag. 108, 30–42. https://doi.org/10.1016/j.enconman.2015.11.009

Patnaik, V., Perez-Blanco, H., 1994. Counter flow heat-exchanger analysis for the design of falling film absorbers, in: International Absorption Heat Pump Conference, January 19-21. ASME, pp. 209–216.

SIMA, 2019. Monterrey climatic conditions of the 23 July 2018 (personal contact).

Vargas Bautista, J.P., García Cuéllar, A.J., Rivera Solorio, C.I., 2011. Design and economic analysis of a solar air-conditioning system: case of study in Monterrey, Mexico, in: EUROSUN 2011.

Venegas, M., Arzoz, D., Rodríguez, P., Izquierdo, M., 2003. Heat and mass transfer in $LiNO_3$-NH_3 spray absorption system. Int. Commun. Heat Mass Transf. 30, 805–815. https://doi.org/10.1016/S0735-1933(03)00128-3

Ventas, R., Lecuona, A., Legrand, M., Rodríguez-Hidalgo, M.C., 2010. On the recirculation of ammonia-lithium nitrate in adiabatic absorbers for chillers. Appl. Therm. Eng. 30, 2770–2777. https://doi.org/10.1016/j.applthermaleng.2010.08.001

Wang, L., Sundén, B., Manglik, R.M., 2007. Plate Heat Exchangers. Design, Applications and Performance. Wit Press. https://doi.org/10.1081/E-EAFE

Wu, W., Wang, B., Shi, W., Li, X., 2014. An overview of ammonia-based absorption chillers and heat pumps. Renew. Sustain. Energy Rev. 31, 681–707. https://doi.org/10.1016/j.rser.2013.12.021

Yuan, Z., Herold, K.E., 2005. Thermodynamic properties of aqueous lithium bromide using a multiproperty free energy correlation. HVAC R Res. 11, 377–393. https://doi.org/10.1080/10789669.2005.10391144

Zhu, L., Gu, J., 2010. Second law-based thermodynamic analysis of ammonia/sodium thiocyanate absorption system. Renew. Energy 35, 1940–1946. https://doi.org/10.1016/j.renene.2010.01.022